Journal of
Applied & Computational Mathematics

Liu et al., J Appl Computat Math 2013, 2:4
DOI: 10.4172/2168-9679.1000136

Research Article Open Access

Spectral Element Simulation of Reaction-Diffusion System in the Neuromuscular Junction

Don Liu*[1], Yifan Wang[1] and Mark A DeCoster[2]

[1]*Mathematics and Statistics, Louisiana Tech University, Ruston, LA 71272, USA*
[2]*Biomedical Engineering, Louisiana Tech University, Ruston, LA 71272, USA*

Abstract

Studying the synaptic signal transmission in the neuromuscular junction (NMJ) is central to the understanding of neuromuscular disorders such as myasthenia gravis disease. Investigating the dynamics of acetylcholine and acetylcholine receptors in an NMJ under the conditions of activated enzyme is an important step towards this mission. In this article, we developed a numerical model of high order accuracy for complex geometry to simulate the complex processes in an NMJ cleft. This model has a full description of three-dimensional reaction and diffusion processes with nonlinear reaction source terms and is capable of predicting the concentration rates of acetylcholine with receptors and enzymes. Simulation results agree with experimental measurement of the reported maximum number of open receptors during the course of a normal action potential. The time variation of populations of open receptor as well as concentration rates are investigated and discussed. This model has the potential to further the in depth investigation of dynamics within an NMJ.

Keywords: Reaction; Diffusion; Neuromuscular junction; Parabolic equation; Spectral element method

Introduction

Human cells communicate with each other through structural interfaces known as synapses. All human and animal movements start from synapses connecting a neuron and a muscle cell. This process happens at the neuromuscular junction (NMJ). Since the function of NMJ is very important, it has been extensively studied and is among the best characterized biological synapses. Several events comprise the signal process occurring in NMJ. Vesicles containing the neurotransmitter acetylcholine (Ach) (in humans) molecules fuse with the pre-synaptic membrane. The transmitters diffuse throughout the volume of the cleft and react with acetyl-cholinesterase (E, AE, acE) and acetylcholine receptors (R). Acetylcholinesterase is an enzyme which destroys Ach and limits its presence in the cleft. Various Ach receptors are embedded in the post-synaptic membrane. The binding of Ach to the Ach receptors causes the opening and closing of the Ach receptor channels (A_2R, A_2R_{open}). These channels allow exchange of potassium and sodium ions, which causes an end-plate current to initiate in the post-synaptic region. Ach molecules which do not encounter AchE are eventually diffused out of the cleft into surrounding tissues or recycled at the pre-synaptic membrane [1-11].

Many techniques used to measure and describe NMJ processes are invasive and must be judiciously applied to prevent significantly disturbance of the function of NMJ [1,6-9,12]. Therefore, mathematical models for NMJ processes have been developed to analyze NMJ processes, which are difficult to measure with a direct experiment [13-22]. The dynamic diffusion of Ach through the synaptic gap and the reactions of Ach with receptors at the end-plate as well as with AchE are crucial fundamentals of NMJ transmission process. This transmission process is essentially coupled diffusion and chemical reactions. The mathematical approach for analyzing this process is to solve the reaction-diffusion equations. Reaction-diffusion processes are studied with systems of coupled nonlinear partial differential equations (PDE). Nonlinear PDE in complex geometries are analytically intractable. Only a few simplified analytical models of NMJ processes [16,21,22] have been developed so far. Despite their contributions, these analytical models either do not incorporate complete reaction kinetics or simplify the geometry and the spatial dimensions. Numerical methods are viable for providing solutions to complex systems [13-20,23-24]. Over the last thirty years, several important models using reaction-diffusion kinetics to study the dynamics of synaptic chemical transmission have been published. Results revealed interesting results and advanced our understanding of NMJ processes [14,19,23,24]. In Khaliq et al. [25], a three dimensional (3D) model of reaction-diffusion processes occurring in the NMJ was presented. The system is simplified as a right cylinder using cylindrical coordinates. However in reality, NMJ actually occurs in rather complex geometry. In addition, active enzyme reactions do exist in NMJ. Inclusion of activated enzyme reactions is particularly important for a normal physical neuromuscular system. Therefore, in this paper, we consider the complex chemistry in NMJ associated with the reaction diffusion processes in complex geometry and conduct an indepth investigation of the mechanisms within NMJ. In terms of numerical methods, Kaihsu [26] and Cheng et al. [27] simulated NMJ with finite element method (FEM). Unfortunately, a general FEM is limited in reaching high order accuracy, aside from using smaller and more elements, as the basis functions are not orthogonal to each other. To achieve high resolution and accuracy, our model uses a spectral element method (SEM) in this paper. For the first time ever, the spectral accuracy and exponential convergence are provided for investigating the complex reaction diffusion system. SEM, a high order finite element method, first appeared in [28], could achieve high resolution with much less elements than a standard FEM. SEM has the capability of hp-refinement, especially the p-type discretization

***Corresponding author:** Don Liu, Mathematics and Statistics, Louisiana Tech University, Ruston, LA 71272, USA; Tel: 318 257 4670; E-mail: DonLiu@LATech.edu

Received August 18, 2013; **Accepted** September 12, 2013; **Published** September 18, 2013

Citation: Liu D, Wang Y, DeCoster MA (2013) Spectral Element Simulation of Reaction-Diffusion System in the Neuromuscular Junction. J Appl Computat Math 2: 136. doi:10.4172/2168-9679.1000136

provides enhanced spatial resolution and flexibility as demonstrated in computational fluid dynamics and two-phase flow simulations [29-37]. In this paper, we propose a three dimensional model implemented with a nodal Galerkin spectral element method using orthogonal Lagrangian interpolants (on zeros of orthogonal polynomials) as basic functions. This model is used to simulate the complex chemistry with enzymes and reaction-diffusion processes in NMJ. The advantage of this model is that it not only resolves strong diffusivity and stiffness from reaction terms, but also provides spectral accuracy in the numerical solution for the associated complex geometry. Simulation results are discussed and compared with results from other researchers. The accuracy of this simulation model is illustrated.

NMJ Model

The neuromuscular junction (NMJ) is a three-dimensional (3D) complex reaction-diffusion system. The geometry of a synaptic cleft of the NMJ is similar to a flat cylindrical fork. The end of a pre-synaptic axon forms a knoblike bulge structure called terminal bouton. The membrane of the bouton is relatively smooth. However, the sarcolemma, i.e., the cell membrane of a post-muscle cell, contains invaginations which is called post junctional folds, and constitutes a rough surface [38]. According to [38], the gap between the flat pre-synaptic membrane and the jagged post-synaptic membrane is about 30 nm. Therefore, a NMJ is approximated as a flat cylindrical fork here. The synaptic gap, bounded by the pre-synaptic membrane at the top and post-synaptic membrane (also called end-plate) at the bottom, is accessible to the external environment at the edge, as shown in Figure 1. The complex biochemistry and processes are well explained in [12,39-42]. To simulate the reactions and processes within an NMJ, a series of 3D mesh for the NMJ cleft were generated, one of them is shown in Figure 2. In order to explain the structure and the mechanism of the NMJ system, the mesh is turned upside down in this figure to demonstrate the shape of the post-synaptic membrane and the reactions of the Acetylcholine (Ach) receptors. The neurotransmitter acetylcholine is released at the center of the pre-synaptic membrane and is diffused across the NMJ cleft. All kinds of immobile neuromuscular receptors are located at the post-synaptic membrane. Aetylcholinesterase (AchE), an enzyme which hydrolyzes the neurotransmitter acetylcholine, is filled in the cleft. AchE is an extracellular matrix molecule [43] that concentrates on the post-synaptic membrane through binding. According to the research in [27,44], AchE is different from the Ach receptors which are embedded at the post-synaptic membrane; it is suspended by the collagen stalks which bound to the muscle membrane (post-membrane). The main function of AchE is to degrade Ach so that much fewer Ach can reach Ach receptors and the process of neurotransmission terminates. Because

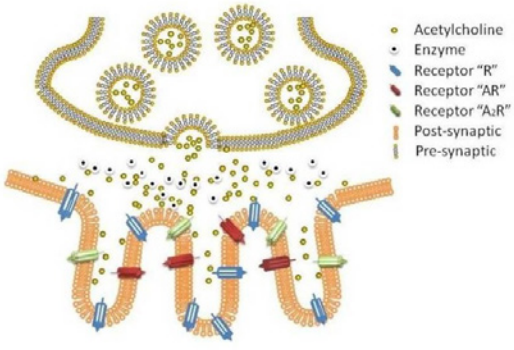

Figure 1: Demonstration of a typical neuromuscular junction.

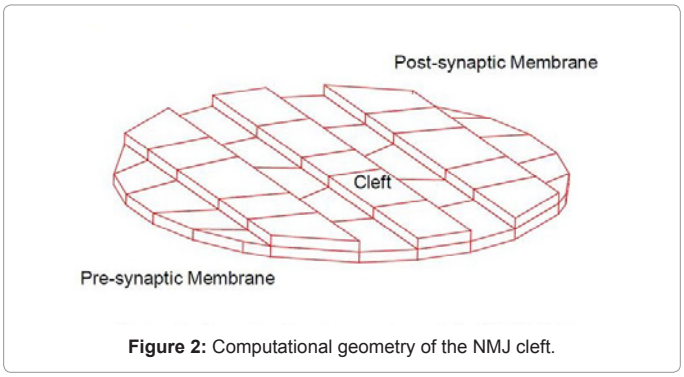

Figure 2: Computational geometry of the NMJ cleft.

the synaptic cleft is very thin (30 nm), for convenience, we simplified the distribution of AchE as all over the cleft. This simplification does not affect its function as hydrolyzing Ach and thus does not influence overall results.

In the governing partial differential equations (PDE) of the simulation model, we consider the following chemical reactions involving AchE:

$$A + E \underset{k_{-E1}}{\overset{k_{E1}}{\rightleftharpoons}} AE \tag{1}$$

$$AE \xrightarrow{k_{E2}} acE \tag{2}$$

$$acE \xrightarrow{k_{E3}} E \tag{3}$$

where A, E, AE, acE represent the acetylcholine, acetyl-cholinesterase, Michaelis ligand-substrate complex, and acylate enzyme, respectively; and k_{E1}, k_{-E1}, k_{E2}, k_{E3} are the forward and backward reaction constants for E, AE, acE, respectively. In a normal NMJ activity, the enzymatic destruction of acetylcholine by AchE is an important reaction. Our model has included all essential and fundamental processes which constitute the production, transmission and enzymatic destruction of acetylcholine involved in a neuromuscular action potential. The schematic reaction Equation (1), (2), and (3) represent the full kinetic cycle of acetylcholine initially reacting with acetylcholinsesterase and then proceeding to the final renewal of the enzyme. The reaction rates of the chemical reaction equations involving enzyme, as given above, are governed by the following ordinary differential equations:

$$\frac{\partial(E)}{\partial t} = -k_{E1}(A)(E) + k_{-E1}(AE) + k_{E3}(acE) \tag{4}$$

$$\frac{\partial(AE)}{\partial t} = k_{E1}(A)(E) - k_{-E1}(AE) - k_{E2}(AE) \tag{5}$$

$$\frac{\partial(acE)}{\partial t} = -k_{E3}(acE) + k_{E2}(AE) \tag{6}$$

The acetylcholine is transported across the cleft and reacts with receptors located on the post-synaptic membrane. We expressed the rate change of concentration for the acetylcholine in a reaction-diffusion equation with variable source terms in a Cartesian system:

$$\frac{\partial(A)}{\partial t} = D_x\frac{\partial^2 A}{\partial x^2} + D_y\frac{\partial^2 A}{\partial y^2} + D_z\frac{\partial^2 A}{\partial z^2} - 2k_R(A)(R) + k_{-R}(AR) - k_{AR}(A)(AR) + 2k_{-AR}(A_2R) - k_{E1}(A)(E) + k_{-E1}(AE) \tag{7}$$

where D_x, D_y, D_z are diffusion coefficients in the x, y, z directions, respectively; and R, AR, A_2R stand for unbound, single and double bound closed acetylcholine receptors.

These equations take into consideration the importance of

acetylcholine breakdown by acetyl-cholinesterase, which has a very high catalytic activity, consistent with its role in nervous function [45,46]. This model is capable of investigating anisotropic diffusion in NMJ. Therefore, different symbols for diffusion coefficients in different directions are used in Equation (7). However, a single constant was actually used in our computation. The practical measurement of the diffusion coefficients involved here is discussed in [47-50]. After the non-dimensionalization, which is given in the Appendix, we rescaled the geometry as $0 \le x, y \le 5$ and $0 \le z \le 0.5$. Other dimensionless coefficients are given in the Appendix.

The boundary conditions for A are specified as:

$$\frac{\partial A(x,y,0,t)}{\partial z}=0 \tag{8}$$

$$\frac{\partial A(x,y,0.5,t)}{\partial z}=0 \tag{9}$$

$$A(x,y,z,t)=0 \quad for \quad x^2+y^2=5^2 \tag{10}$$

The initial conditions for A, R, E are given as:

$$A(x,y,z,0)=A_0 \tag{11}$$

$$R(x,y,z,0)=R_0 \tag{12}$$

$$E(x,y,z,0)=E_0, \quad where \quad 0 \le z \le 0.5 \tag{13}$$

The above parabolic system with activated enzyme in the complex geometry is solved numerically to predict the concentration evolution of acetylcholine under normal neuromuscular operations. The above parabolic system with activated enzyme in the complex geometry is solved numerically to predict the concentration evolution of acetylcholine under normal neuromuscular operations.

Numerical Method

To obtain high accuracy in time, the ordinary differential equations (4), (5), and (6) for E, AE, acE are solved with the fourth order Runge-Kutta scheme. We demonstrate the procedure for E only as the rest is similar:

$$E_g^{n+1}=E_g^n+\frac{E_{rk1}+2E_{rk2}+2E_{rk3}+E_{rk4}}{6} \tag{14}$$

where the subscript g stands for global value, the subscript rk_1 represents the first step in Runge-Kutta scheme, etc. The coefficients E_{rk1}, E_{rk2}, E_{rk3}, E_{rk4} are determined as below:

$$E_{rk1}=\Delta t\left[-k_{E1}\left(\frac{A_g^{n+1}+A_g^n}{2}\right)E_g^n+k_{\_E1}\left(AE_g^n\right)+k_{E3}\left(acE_g^n\right)\right] \tag{15}$$

$$E_{rk2}=\Delta t\left[-k_{E1}\left(\frac{A_g^{n+1}+A_g^n}{2}\right)\left(E_g^n+\frac{E_{rk1}}{2}\right)+k_{\_E1}\left(AE_g^n+\frac{AE_{rk1}}{2}\right)+k_{E3}\left(acE_g^n+\frac{acE_{rk1}}{2}\right)\right] \tag{16}$$

$$E_{rk3}=\Delta t\left[-k_{E1}\left(\frac{A_g^{n+1}+A_g^n}{2}\right)\left(E_g^n+\frac{E_{rk2}}{2}\right)+k_{\_E1}\left(AE_g^n+\frac{AE_{rk2}}{2}\right)+k_{E3}\left(acE_g^n+\frac{acE_{rk2}}{2}\right)\right] \tag{17}$$

$$E_{rk4}=\Delta t\left[-k_{E1}\left(\frac{A_g^{n+1}+A_g^n}{2}\right)\left(E_g^n+\frac{E_{rk3}}{2}\right)+k_{\_E1}\left(AE_g^n+\frac{AE_{rk3}}{2}\right)+k_{E3}\left(acE_g^n+\frac{acE_{rk3}}{2}\right)\right] \tag{18}$$

Where, AE_{rk} and acE_{rk} are chemical compound Michaelis ligand-substrate complex and acylate enzyme in corresponding steps in Runge-Kutta scheme.

In space, a Galerkin projection was used to obtain the variational form of the Equation (7). Then a spectral element discretization was used to obtain numerical solutions in complex geometry. The Crank-Nicholson scheme was implemented in time. For any element, labeled as e, in the original Cartesian coordinates, as shown in Figure 2, we map it to a standard element in ξ_0, ξ_2, ξ_3, and then expand the solution for A in Equation (7) in terms of a tensor product of three one-dimensional Lagrangian polynomials on quadrature points, which are chosen to be zeros of Legendre polynomials:

$$A^e(\xi_1,\xi_2,\xi_3)=\sum_p^{Po}\sum_q^{Po}\sum_r^{Po}A^e_{pqr}h^e_p(\xi_1)h^e_q(\xi_2)h^e_r(\xi_3)=\sum A^e_{pqr}\Phi^e_{pqr} \tag{19}$$

where, Po is the highest polynomial order of basic functions, which ranges from 2 to 20. For convenience, we chose the same Po in x, y, z directions, although they could be different according to specific conditions. Because of the collocation property of the nodal SEM, coefficients of basic functions are the numerical solutions at quadrature points. This is convenient in computing the nonlinear term and the reason we chose nodal basis instead of modal basis functions. Those reaction terms in Equation (7) can be represented as:

$$\left[(A)(R)\right]^e(\xi_1,\xi_2,\xi_3)=\sum_{pqr}\left[\left(A_{pqr}\right).*\left(R_{pqr}\right)\right]^e\Phi^e_{pqr} \tag{20}$$

$$\left[(A)(AR)\right]^e(\xi_1,\xi_2,\xi_3)=\sum_{pqr}\left[\left(A_{pqr}\right).*\left(AR_{pqr}\right)\right]^e\Phi^e_{pqr} \tag{21}$$

$$\left[(A_2R)\right]^e(\xi_1,\xi_2,\xi_3)=\sum_{pqr}\left[\left(A_2R\right)_{pqr}\right]^e\Phi^e_{pqr} \tag{22}$$

$$\left[(A)(E)\right]^e(\xi_1,\xi_2,\xi_3)=\sum_{pqr}\left[\left(A_{pqr}\right).*\left(E_{pqr}\right)\right]^e\Phi^e_{pqr} \tag{23}$$

$$\left[(AE)\right]^e(\xi_1,\xi_2,\xi_3)=\sum_{pqr}\left[\left(AE\right)_{pqr}\right]^e\Phi^e_{pqr} \tag{24}$$

where, the superscript e stands for the elemental solutions. For nonlinear terms, the coefficients were calculated in point-wise product of values of two species on quadrature points. We denoted this operation as.*in Equation (20), (21), (22), (23), and (24). Specifically, we use Equation (20) to illustrate this implementation. The nonlinear product (A) (R) at a quadrature point $\xi_{ijk}=(\xi_i, \xi_j, \xi_k)$ are computed as below:

$$\left[(A)(R)\right]^e(\xi_i,\xi_j,\xi_k)=\left[\left(A_{pqr}\right)\right]^e\Phi^e_{pqr}(i,j,k)\left[\left(R_{lmn}\right)\right]^e\Phi^e_{lmn}(i,j,k) \tag{25}$$

Due to the property of δ function:

$$\Phi_{pqr}(i,j,k)=\ _{pqr\ ijk}=\begin{cases}1, & p=i,q=j,r=k\\ 0, & Otherwise\end{cases} \tag{26}$$

and

$$\Phi^e_{lmn}(i,j,k)=\delta_{lmn,ijk}=\begin{cases}1, & l=i,m=j,n=k\\ 0, & Otherwise\end{cases} \tag{27}$$

Equation (25) can be approximated as:

$$\left[(A)(R)\right]^e(\xi_i,\xi_j,\xi_k)=\left[\left(A_{pqr}\right)\right]^e\left[\left(R_{pqr}\right)\right]^e\Phi^e_{pqr}(i,j,k)=\left[\left(A_{pqr}\right).*\left(AR_{pqr}\right)\right]^e\Phi^e_{pqr}(i,j,k) \tag{28}$$

The basis function in a standard element in tensor form is then:

$$\Psi^e_{lmn}=\sum_l^{Po}\sum_m^{Po}\sum_n^{Po}h^e_l(\xi_1)h^e_m(\xi_2)h^e_n(\xi_3) \tag{29}$$

By a Galerkin projection, the weak form of Equation (7) could be obtained. After a global assembly, we obtain the linear system of Equation (7) in the matrix-vector form:

$$\underline{\underline{M}}\frac{\partial A_g}{\partial t}=-\underline{\underline{K}}A_g-2k_R\underline{\underline{M}}\left[\left(A_g\right).*\left(R_g\right)\right]+k_{-R}\underline{\underline{M}}\left(AR_g\right)-k_{AR}\underline{\underline{M}}\left[\left(A_g\right).*\left(AR_g\right)\right]+2k_{-AR}\underline{\underline{M}}\left(A_2R\right)_g \\ -k_{E1}\underline{\underline{M}}\left[\left(A_g\right).*\left(E_g\right)\right]+k_{-E1}\underline{\underline{M}}\left(AE\right)_g \quad (30)$$

Where $\underline{\underline{M}}$ is the global mass matrix:

$$\underline{\underline{M}}=\sum_e^n\left(\int_{\Omega_e}\Phi^e_{pqr}\Psi^e_{lmn}\left|J\right|_e d\xi_1 d\xi_2 d\xi_3\right) \quad (31)$$

Where $|J|_e$ is the Jacobian of the element e; Ω_e is the integral domain; and N is the total number of elements. The diffusion matrix $\underline{\underline{K}}$ consists of contributions from all directions:

$$\underline{\underline{K}}=\sum_e^N\begin{Bmatrix}D_x\int_{\Omega_e}\left(\Phi^e_{pqr}\right)'_x\left(\Psi^e_{lmn}\right)'_x\left(\frac{\partial x_2}{\partial\xi_2}\frac{\partial x_3}{\partial\xi_3}-\frac{\partial x_2}{\partial\xi_3}\frac{\partial x_3}{\partial\xi_2}\right)\left|J\right|_e^{-1}\partial\xi_1\partial\xi_2\partial\xi_3 \\ +D_y\int_{\Omega_e}\left(\Phi^e_{pqr}\right)'_y\left(\Psi^e_{lmn}\right)'_y\left(\frac{\partial x_1}{\partial\xi_1}\frac{\partial x_3}{\partial\xi_3}-\frac{\partial x_1}{\partial\xi_3}\frac{\partial x_3}{\partial\xi_1}\right)\left|J\right|_e^{-1}\partial\xi_1\partial\xi_2\partial\xi_3 \\ +D_z\int_{\Omega_e}\left(\Phi^e_{pqr}\right)'_z\left(\Psi^e_{lmn}\right)'_z\left(\frac{\partial x_1}{\partial\xi_1}\frac{\partial x_2}{\partial\xi_2}-\frac{\partial x_1}{\partial\xi_2}\frac{\partial x_2}{\partial\xi_1}\right)\left|J\right|_e^{-1}\partial\xi_1\partial\xi_2\partial\xi_3\end{Bmatrix} \quad (32)$$

We use the Crank-Nicholson scheme for Equation (30):

$$\underline{\underline{M}}\frac{A_g^{n+1}-A_g^n}{\Delta t}=-\underline{\underline{K}}\left(\frac{A_g^{n+1}+A_g^n}{2}\right)-2k_R\underline{\underline{M}}\left[\left(\frac{A_g^{n+1}+A_g^n}{2}\right).*\left(\frac{R_g^{n+1}+R_g^n}{2}\right)\right] \\ +k_{-R}\underline{\underline{M}}\left(\frac{\left(AR\right)_g^{n+1}+\left(AR\right)_g^n}{2}\right)-k_{AR}\underline{\underline{M}}\left[\left(\frac{A_g^{n+1}+A_g^n}{2}\right).*\frac{\left(AR\right)_g^{n+1}+\left(AR\right)_g^n}{2}\right] \\ +2k_{-AR}\underline{\underline{M}}\left[\left(\frac{\left(A_2R\right)_g^{n+1}+\left(A_2R\right)_g^n}{2}\right)-k_{E1}\underline{\underline{M}}\left(\frac{A_g^{n+1}+A_g^n}{2}\right).*\left(\frac{E_g^{n+1}+\left(E\right)_g^n}{2}\right)\right] \quad (33) \\ +k_{E1}\underline{\underline{M}}\left(\frac{\left(AE\right)_g^{n+1}+\left(AE\right)_g^n}{2}\right)$$

The major computational procedures for values of chemical compounds at the next time level n+1 based on the present level n are given below:

• Initialize values of compounds A, R, AR, A2R, $A2R_{open}$, E, AE, acE at the time level n+1 with the same values at the time step n;

• Apply the Runge-Kutta scheme to obtain the values of R,AR,A2R,A2Ropen,E, AE, acE at the time level n+1;

• Substitute updated values of A, R, AR, A2R, $A2R_{open}$, E, AE, acE from step 2 into Equation (33), then solve for the value of A at the time level n+1;

• Repeat steps 1 to 3, until the overall difference between two adjacent values of A is within the tolerance 1.0×10^{-12}.

Numerical Results

A nodal spectral element method was implemented for numerical solution. Since the expansion order of basic functions relies on quadrature nodes, as the polynomial order increases, different nodal points are actually used. Figure 3 shows the top views of NMJ in the cross section at the plane z=0, with the highest polynomial order varying from 3, 4, to 5. The red lines are the boundaries of elements. The intersections of blue lines are actual quadrature points within each element. Zeros of Legendre polynomials are used as quadrature points since they cluster near boundaries naturally and help minimize discretization error.

Figure 4 illustrates the side views of the computational domain in

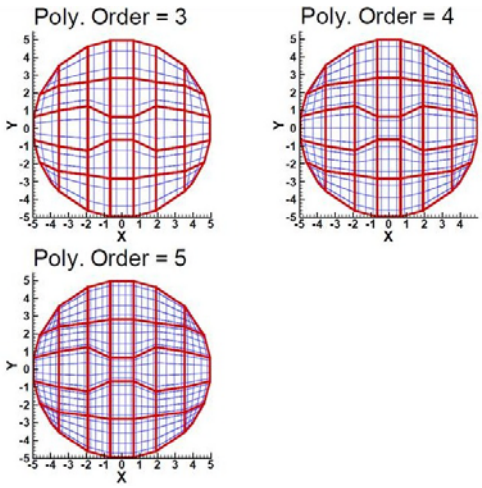

Figure 3: Computational mesh at different polynomial orders in the plane Z=0 for NMJ.

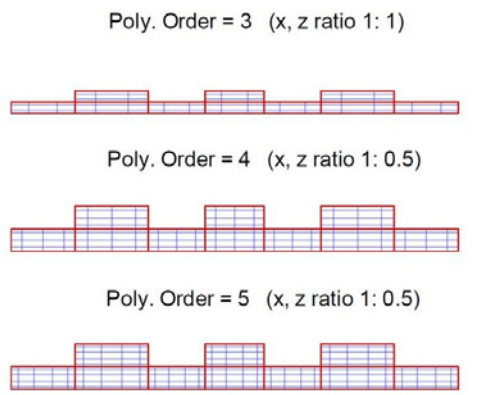

Figure 4: Computational mesh at different polynomial orders in the plane Y=0 for NMJ.

the middle cross section (plane y=0) of NMJ with polynomial order being 3, 4 and 5. To better visualize the mesh, we exaggerated the ratio in z direction for the cases of 4^{th} and 5^{th} order expansion. This is because the synaptic cleft is very thin and when polynomial order is beyond five, quadratur epoints are crowded together in the plot and look like as if they were uniformly distributed. Since the diffusion process of the neurotransmitter acetylcholine mainly happens in the NMJ cleft, the contour lines of its concentration in the cross sectional plane of Y=0 are presented in four snapshots in Figure 5 to show the change in the concentration of acetylcholine in NMJ. Because the characteristic length, the thickness of an NMJ is of several orders of magnitude larger than the mean free path, the diffusion rate should be the same in all directions. In our numerical simulation results, we have observed that the diffusion rates along all directions are almost the same. If the effects of confinement and in homogeneity are necessary to be considered, our model is fully capable of describing different diffusion rates in space.

Predicting the number of open receptors as time goes by is an important indicator for an accurate model. Available references [24,39,51] have reported that the maximum number of open receptors during the course of a normal action potential is about 2000 at 0.3 ms. Our predicted time evolution of A_2R_{open} in the NMJ, at varied spatial

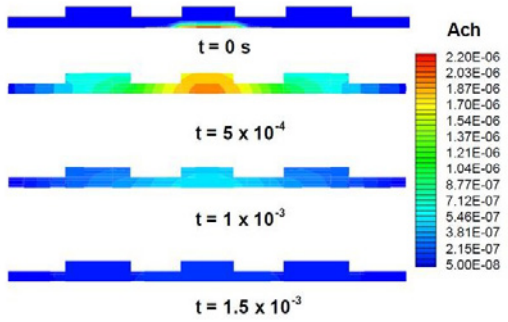

Figure 5: Evolution of the concentration of Acetylcholine in the plane Y=0.

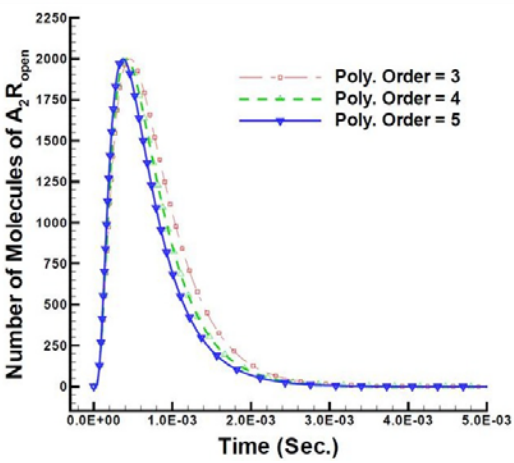

Figure 6: Evolution of the number of molecules of A_2R_{open} in the entire Neuromuscular Junction.

Name	Value (Unit)	Explanation
k_R	$3.0\times10^{7}\,Mol^{-1}s^{-1}$	Forward rate of reaction of R
k_{-R}	$1.0\times10^{4}\,s^{-1}$	Backward rate of reaction of R
k_{AR}	$3.0\times10^{7}\,Mol^{-1}s^{-1}$	Forward rate of reaction of AR
k_{-AR}	$1.0\times10^{4}\,s^{-1}$	Backward rate of reaction of AR
k_{E1}	$2.0\times10^{8}\,Mol^{-1}s^{-1}$	Forward rate of reaction of AE
k_{-E1}	$1.0\times10^{3}\,s^{-1}$	Backward rate of reaction of AE
k_{E2}	$1.1\times10^{5}\,s^{-1}$	Forward rate of reaction of acE
k_{E3}	$2.0\times10^{4}\,s^{-1}$	Forward rate of reaction of E
D_x	$1.0\times10^{-6}\,cm^2/s$	Diffusion rate in x direction
D_y	$1.0\times10^{-6}\,cm^2/s$	Diffusion rate in y direction
D_z	$1.0\times10^{-6}\,cm^2/s$	Diffusion rate in z direction
R	$5.0\times10^{-5}\,cm$	Radius of NMJ cleft
L	$5.0\times10^{-6}\,cm$	Depth of NMJ cleft
Num	$6.02\times10^{23}\,mol^{-1}$	Number of Molecules per Mol

Table 1: The coefficients of the NMJ reaction-diffusion system.

resolution, is shown in Figure 6. It is obvious that the number of A_2R_{open} increases rapidly during an initial transient

period to reach its maximum at about 0.4ms, and then gradually decreases. After 3×10^{-3} it dissipates away. This trend agrees with the experimental data from [26,27]. Table 1 in the Appendix lists the parameters of geometry, reaction rate constants, diffusion coefficients, and other parameters in the model.

To further demonstrate the evolution of double-bounded open acetylcholine receptors (A_2R_{open}) located at the post-synaptic membrane, we present the contour plots of the concentration of A_2R_{open} versus time in Figures 7-9. Because the most significant reaction and diffusion happen from the initial moment to 1.5 ms, we only focus on the time interval from 0 to 1.5 ms. The variation of the concentration of acetylcholine is similar to the trend in Figure 6. Due to the strong dissipation, the peak concentration of acetylcholine fades away quickly.

Conclusion

We have developed a full three dimensional model with realistic geometry using spectral nodal element method, a high order finite element method. The dynamics of the reaction-diffusion of acetylcholine and acetylcholine receptors are presented in the neuromuscular junction under conditions of activated enzyme. The assumption we used is a uniform distribution of acetylcholine receptors at post-synaptic membrane, which is accepted and used in open literature. Our results are in agreement with literature. The maximum number of open receptors during the course of a normal action potential is predicted to be around 2000 at approximately 0.4 ms. With spectral accuracy, our model allows us to see the entire process and all local details of a normal NMJ activity. Besides, it provides a means to investigate complex processes such as how an abnormal distribution could affect the receptor dynamics

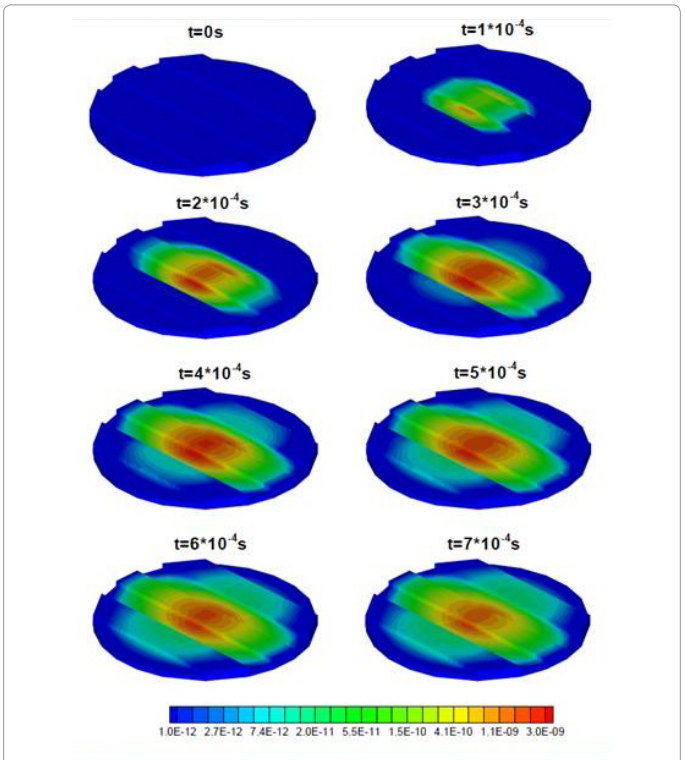

Figure 7: Evolution of the concentration of A_2R_{open} at post-synaptic membrane: Part 1.

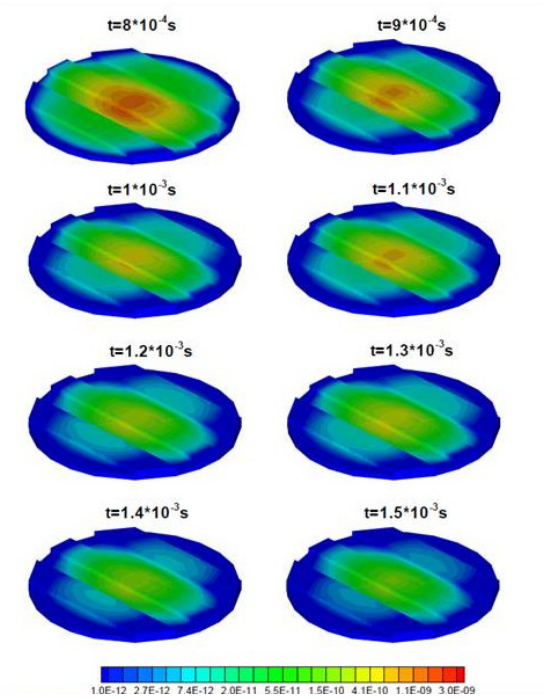

Figure 8: Evolution of the concentration of A_2R_{open} at post-synaptic membrane: Part 2.

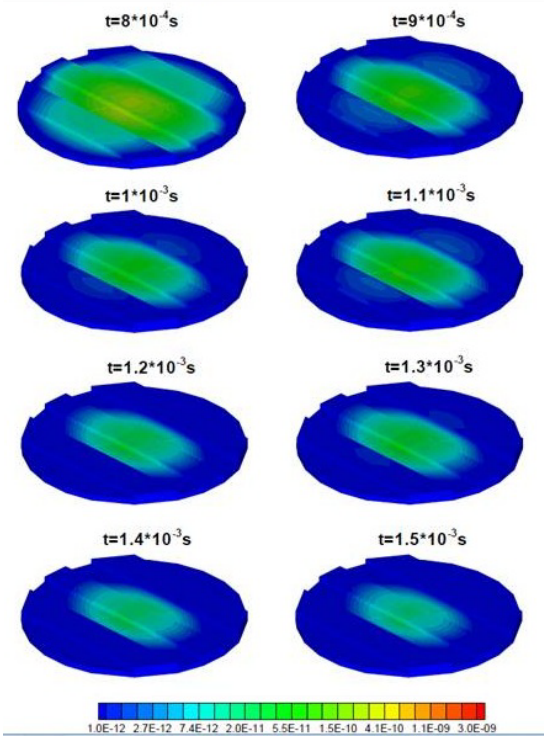

Figure 9: Evolution of the concentration of A_2R_{open} at post-synaptic Membrane: Part 3.

during an action potential by systematically varying the distribution of acetylcholine receptors according to the actual biomedical situations. Besides, our model is capable of studying the sensitivity of the dynamics of open receptors to changes in anisotropic diffusion parameters. In addition, our model can analyze the subsequent effects of open receptor distribution when acetylcholine receptors are non-uniformly distributed at the post-synaptic membrane. Future investigations will focus on the study of an organophosphate neurotoxin entering the cleft from the outer periphery and enzyme regeneration with oxime therapy.

Appendix

Non-dimensionalization

The coefficients of the NMJ reaction-diffusion system are listed in Table 1:

In Table 1, we found out that coefficients range from 10^{-6} to 10^{7}, spanning almost the entire range of double decision accuracy. Therefore, all equations were non-dimensionalized before computation starts in order to avoid large rounding error. We set the characteristic length scale to be $L_s=10^{-5}$ cm and chose the characteristic diffusion rate $D_s=10^{-10}$ cm^2/s, so that the numbers are not too large and not too small. The non-dimensional values are:

$$L' = \frac{L}{L_s} = 5$$

$$R' = \frac{R}{L_s} = 0.5$$

$$D_x' = D_y' = D_z' = \frac{D_x}{D_s} = 1 \times 10^4$$

$$T' = \frac{L_s^2}{D_s} = \frac{10^{-10}}{10^{-10}} = 1$$

Especially, we want the scaled time to be unit so that temporal error is reduced significantly. The reaction rates in the table are scaled accordingly as they are constant, although variable reaction rates could be used in our model.

Acknowledgement

This study was supported by National Science Foundation under grants DMS-1115546, DMS-1318988.

References

1. Anderson CR, Stevens CF (1973) Voltage clamp analysis of acetylcholine produced end-plate current fluctuations at frog neuromuscular junction. J Physiol 235: 655-691.
2. Barry PH, Lynch JW (2005) Ligand-gated channels. IEEE Trans Nanobioscience 4: 70-80.
3. Beers WH, Reich E (1970) Structure and activity of acetylcholine. Nature 228: 917-922.
4. Forsberg A, Puu G (1984) Kinetics for the inhibition of acetylcholinesterase from the electric eel by some organophosphates and carbamates. Eur J Biochem 140: 153-156.
5. Hartzell HC, Kuffler SW, Yoshikami D (1975) Post-synaptic potentiation: interaction between quanta of acetylcholine at the skeletal neuromuscular synapse. J Physiol 251: 427-463.
6. Hess GP, Andrews JP (1977) Functional acetylcholine receptor--electroplax membrane microsacs (vesicles): purification and characterization. Proc Natl Acad Sci USA 74: 482-486.
7. Kordas M (1972) An attempt at an analysis of the factors determining the time course of the end-plate current. Journal of Physiology 224: 317-332.
8. Kordas M (1977) On the role of junctional cholinesterase in determining the time course of the end-plate current. J Physiol 270: 133-150.
9. Magleby KL, Terrar DA (1975) Factors affecting the time course of decay of end-plate currents: a possible cooperative action of acetylcholine on receptors at the frog neuromuscular junction. J Physiol 244: 467-495.

10. Miledi R, Molenaar PC, Polak RL (1984) Acetylcholinesterase activity in intact and homogenized skeletal muscle of the frog. J Physiol 349: 663-686.

11. Truskey G (2003) Transport phenomena in biological systems. New Jersey: Prentice Hall.

12. Aidley D (1998) The Physiology of Excitable Cells. Cambridge University Press, J of Experimental Biology, 2nd Ed. 78.

13. Bartol TM Jr, Land BR, Salpeter EE, Salpeter MM (1991) Monte Carlo simulation of miniature endplate current generation in the vertebrate neuromuscular junction. Biophys J 59: 1290-1307.

14. Friboulet A, Thomas D (1993) Reaction-diffusion coupling in a structured system: application to the quantitative simulation of endplate currents. J Theor Biol 160: 441-455.

15. Giniatullin RA, Kheeroug LS, Vyskocil F (1995) Modelling endplate currents: dependence on quantum secretion probability and decay of miniature current. Eur Biophys J 23: 443-446.

16. Kleinle J, Vogt K, Lüscher HR, Müller L, Senn W, et al. (1996) Transmitter concentration profiles in the synaptic cleft: an analytical model of release and diffusion. Biophys J 71: 2413-2426.

17. Madsen BW, Edeson RO, Lam HS, Milne RK (1984) Numerical simulation of miniature endplate currents. Neurosci Lett 48: 67-74.

18. Naka T, Sakamoto N (2002) Simulation analysis of the effects of simultaneous release of quanta of Acetylcholine on the end plate current at the neuromuscular junction. Mathematics and Computers in Simulation 59: 87-94.

19. Rosenberry TL (1979) Quantitative simulation of endplate currents at neuromuscular junctions based on the reaction of acetylcholine with acetylcholine receptor and acetylcholinesterase. Biophys J 26: 263-289.

20. Schild JH, Clark JW, Canavier CC, Kunze DL, Andresen MC (1995) Afferent synaptic drive of rat medial nucleus tractus solitarius neurons: dynamic simulation of graded vesicular mobilization, release, and non-NMDA receptor kinetics. J Neurophysiol 74: 1529-1548.

21. Vieth WR, Chotani G (1983) Diffusional/kinetic analysis of the neurotransmission process at the nerve-muscle junction. Ann N Y Acad Sci 413: 114-132.

22. Vieth WR, Ciftçi T (1981) Transport models of the neurotransmitter-receptor interaction. Ann N Y Acad Sci 369: 99-111.

23. Naka T, Shiba K, Sakamoto N (1997) A two-dimensional compartment model for the reaction-diffusion system of acetylcholine in the synaptic cleft at the neuromuscular junction. Biosystems 41: 17-27.

24. Wathey JC, Nass MM, Lester HA (1979) Numerical reconstruction of the quantal event at nicotinic synapses. Biophys J 27: 145-164.

25. Khaliq A, Jenkins F, DeCoster M, Dai W (2011) A new 3D mass diffusion-reaction model in the neuromuscular junction. J Comput Neurosci 30: 729-745.

26. Tai K, Bond SD, MacMillan HR, Baker NA, Holst MJ, et al. (2003) Finite element simulations of acetylcholine diffusion in neuromuscular junctions. Biophys J 84: 2234-2241.

27. Cheng Y, Suen JK, Radic Z, Bond SD, Holst MJ, et al. (2007) Continuum simulations of acetylcholine diffusion with reaction-determined boundaries in neuromuscular junction models. Biophys Chem 127: 129-139.

28. Patera AT (1984) A spectral element method for fluid dynamics: Laminar flow in a channel expansion. Journal of Computational Physics 54: 468-488.

29. Karniadakis GE, Sherwin SJ (2005) Spectral/hp Element Methods for Computational Fluid Dynamics. Oxford University Press.

30. Mathews JH, Fink KK (2004) Numerical Method Using Matlab. Prentice Hall.

31. Pozrikidis C (2005) Introduction to finite and spectral element method using MATLAB. Taylor and Francis Group, LLC.

32. Dong S, Liu D, Maxey MR, Karniadakis GE (2004) Spectral distributed Lagrange multiplier method: Algorithm and Benchmark tests. J Computational Physics 195: 695-717.

33. Liu D, Chen Q, Wang Y (2011) Spectral element modeling of sediment transport in shear flows. J Comput Methods Appl Mech Engrg 200: 1691-1707.

34. Liu D, Lvov Y, Dai W (2011) Joint simulations of confined diffusion inside Nanotubules. J Computational and Theoretical Nanoscience 8: 1-11.

35. Liu D, Maxey MR, Karniadakis GE (2002) A fast method for particulate microflows. J Microelectromechanical System 11: 691-702.

36. Liu D, Maxey MR, Karniadakis GE (2004) Modeling and optimization of colloidal micro-pumps. J. Micromechanics and Microengineering 14: 567-575.

37. Liu D, Maxey MR., Karniadakis GE (2005) Simulations of dynamic self-assembly of paramagnetic microspheres in confined microgeometries. J. Micromechanics and Microengineering 15: 2298-2308.

38. Nicholls JG, Martin AR, Fuchs PA, Brown DA, Diamond ME, et al. (2012) From Neuron to Brain. Sunderland, Mass: Sinauer Associates, 5th Ed.

39. Kandel E (2000) Principles of neuroscience. New York: McGraw-Hill.

40. Junge D (1992) Nerve and muscle excitation. Sunderland: Sinauer Associates Inc.

41. Matthews G (1991) Cellular physiology of nerve and muscle. Blackwell Scientific Publications.

42. Purves D (2001) Neuroscience. Sunderland: Sinauer Associates Inc.

43. Dvir H, Silman I, Harel M, Rosenberry TL, Sussman JL (2010) Acetylcholinesterase: from 3D structure to function. Chem Biol Interact 187: 10-22.

44. Peng HB, Xie H, Rossi SG, Rotundo RL (1999) Acetylcholinesterase clustering at the neuromuscular junction involves perlecan and dystroglycan. J Cell Biol 145: 911-921.

45. Quinn DM (1987) Acetylcholinesterase: enzyme structure, reaction dynamics, and virtual transition states. Chemical Reviews 87: 955-979.

46. WILSON IB, HARRISON MA (1961) Turnover number of acetyl-cholinesterase. J Biol Chem 236: 2292-2295.

47. Grosman C, Salamone FN, Sine SM, Auerbach A (2000) The extracellular linker of muscle acetylcholine receptor channels is a gating control element. J Gen Physiol 116: 327-340.

48. Land BR, Harris WV, Salpeter EE, Salpeter MM (1984) Diffusion and binding constants for acetylcholine derived from the falling phase of miniature endplate currents. Proc Natl Acad Sci USA 81: 1594-1598.

49. Radic Z, Pickering NA, Vellom DC, Camp S, Taylor P (1993) Three distinct domains in the cholinesterase molecule confer selectivity for acetyl- and butyrylcholinesterase inhibitors. Biochemistry 32: 12074-12084.

50. Salamone FN, Zhou M, Auerbach A (1999) A re-examination of adult mouse nicotinic acetylcholine receptor channel activation kinetics. J Physiol 516: 315-330.

51. Lester HA (1977) The response to acetylcholine. Sci Am 236: 106-116.